Two-Dimensional Spectra of Radar Returns From Sea: 2. Analysis of the Group Line From Experimental Data

Florestan Platzer, Marc Saillard, Vincent Fabbro

JGR Oceans

RESEARCH ARTICLE
10.1029/2019JC015123

This article is a companion to Platzer et al. (2019) http://doi.org/10.1029/2019JC015121.

Key Points:
- A comparison of the analytical model of the group line with experimental data has been performed
- In terms of group line, experimental data behave as the square of the slope of the surface
- The group line is not the signature of the breaking waves

Correspondence to:
F. Platzer, M. Saillard, and V. Fabbro,
florestan.platzer@onera.fr;
marc.saillard@univ-tln.fr;
vincent.fabbro@onera.fr

Citation:
Platzer, F., Saillard, M., & Fabbro, V. (2019). Two-dimensional spectra of radar returns from sea: 2. Analysis of the group line from experimental data. *Journal of Geophysical Research: Oceans*, *124*, 8309–8323. https://doi.org/10.1029/2019JC015123

Received 6 MAR 2019
Accepted 25 AUG 2019
Accepted article online 31 OCT 2019
Published online 30 NOV 2019

Two-Dimensional Spectra of Radar Returns From Sea: 2. Analysis of the Group Line From Experimental Data

F. Platzer[1,2], M. Saillard[2], and V. Fabbro[1]

[1]ONERA/DEMR, Université de Toulouse, Toulouse, France, [2]Université de Toulon, Aix Marseille Université, CNRS/INSU, IRD, MIO UM 110, Mediterranean Institute of Oceanography, La Garde, France

Abstract Wavenumber-frequency spectra are obtained by performing a two-dimensional Fourier transform of range-time normalized radar cross-section (NRCS) or Doppler velocity maps. In such diagrams, some energy is present at low space-time frequencies, resulting from the nonlinear behavior of the measured quantity related to the sea surface geometry. This feature is called the group line, since for a narrow-band wave packet the energy is concentrated along a straight line with group velocity as slope. Which physical nonlinear process generates the group line remains an open question. Breaking waves have been proposed as the most probable contributor. However, numerical simulations from weakly nonlinear surfaces without breaking events and experiments performed at low winds also provide such feature. In a companion paper, a theoretical and numerical analysis has permitted to predict the energy distribution of the group line depending on the kind of nonlinearity. It provides some means to characterize a group line in a rigorous way. In this paper, it is used to analyze the group lines derived from the experimental MARLENE data. The group lines computed from the backscattering amplitude behave as the one of the square of sea surface slopes. The analysis of the Doppler velocities provides similar results, which significantly differ from what is expected if breaking waves are the main contributors and do break at velocities reported in the literature. Our results suggest that the group line mainly reflects the asymptotic behavior of the scattering amplitude at grazing incidence, of which the leading nonlinear term is proportional to the square of surface slope.

1. Introduction

Surveillance or navigation radars, designed for detecting targets embedded in sea clutter, can also be used to characterize sea surface waves or surface current. This is often achieved by computing the two- or three-dimensional Fourier transform of high-resolution range-time data (NRCS or Doppler velocity) for various azimuth angles, providing a wavevector-frequency spectrum Borge et al. (2013), Dankert et al. (2005), Smith et al. (1996), Young et al. (1985).

In such dispersion diagrams, a large amount of energy is generally concentrated in the classical dispersion relation of gravity waves $\omega^2 = gk$. Furthermore, a low-frequency feature can be observed, the shape of which looks like a straight piece of line going through the origin. In the literature, it is often referred to as the group line Smith et al. (1996). Its study is the main issue of this paper. Some interpretations have been proposed to explain the physical origin of the group line, such as breaking waves Smith et al. (1996), Frasier and McIntosh (1996), Stevens et al. (1999) or nonlinear scattering effects Frasier and McIntosh (1996), Stevens et al. (1999), Rino et al. (1997).

Plant has also investigated the group line in Plant and Farquharson (2012). He excluded turbulent eddies in the wind, water turbulence advected by currents, and second-order nonlinear interactions from hydrodynamic or electromagnetic waves. The main conclusion is that breaking is the most probable cause of the group line. Then, in Plant (2012), a link is proposed between (i) the slope of the group line simulated from sea surfaces generated with Donelan spectrum Donelan et al. (1985), (ii) the fast scatterers observed in HH Doppler spectra, and (iii) the maximum of Phillips' Lambda function, introduced in Phillips (1985), which describes the distribution of whitecaps on the ocean surface. Hence, the group line was interpreted as the signature of breaking waves.

Space-time series of the backscattered signal have also been generated with a numerical solver based on a rigorous boundary integral formalism Miret, Soriano, Nouguier, et al. (2014). In those simulations, ocean

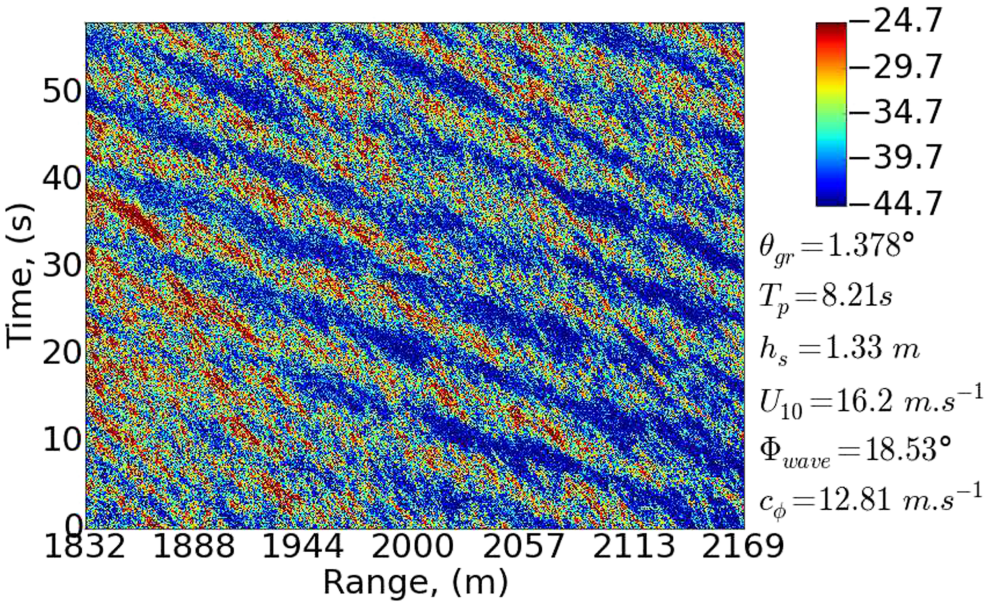

Figure 1. Space-time series of backscattered power (NRCS), in logarithmic scale, acquired by the MARSIG radar (14 GHz). The wind speed is $U_{10} = 16.2$ m/s. θ_{gr} represents the grazing angle, T_p the dominant wave time period, h_s the significant wave height, Φ_{wave} the azimuth angle between the radar pointing direction and the dominant wave direction, and c_ϕ the dominant wave phase speed.

surfaces are described by a Pierson-Moskowitz spectrum combined with Creamer's approach Creamer et al. (1989), and an analysis of Doppler spectra has been performed Miret, Soriano, and Saillard (2014). The dispersion diagram obtained from such numerical simulations (L-band, horizontal polarization), without breaking, also provides a group line Platzer et al. (2019), the slope of which differs from the average Doppler velocity. In the same way, numerical simulations based on nonlinear Schrödinger equation do exhibit such features for weakly nonlinear one-dimensional surfaces Krogstad and Trulsen (2010). This suggests that breaking waves could not be the unique origin of group lines.

Some simple theoretical models that can explain the characteristics of the group lines have been proposed in Platzer et al. (2019). On this basis, the present paper focuses on the group line derived from experimental data and is organized as follows. A description of the MARLENE campaign is introduced in section 2. Section 3 presents a generic method to estimate the slope of a group line from experimental data and its comparison with the theoretical model introduced in Platzer et al. (2019). Then, section 4 provides an analysis of the experimental results and a contribution to the interpretation of the group line. The conclusion and discussions are presented in section 5.

2. Description of the Experiment

The analysis presented in this paper is based on MARLENE campaign, which has been described in Fabbro et al. (2017), together with some analysis of reflectivity and Doppler spectra. The data were obtained in May 2014 with three radar systems called MEMPHIS, MARSIG, and MEDYCIS, deployed on the French south coast. MEMPHIS is a dual-frequency radar (35 and 94 GHz) with a range resolution of 0.75 m and a pulse repetition frequency (PRF) of 10 kHz. The duration of each acquisition was around 60 s. MARSIG, designed by Fraunhofer FHR and operated by WTD71, is a multifrequency radar (8, 11, 14, and 17 GHz simultaneously) with 0.50 m range resolution and an acquisition duration of 60 s with a PRF of 50 Hz. The phase of MARSIG data could not have been exploited. MEDYCIS, developed by ONERA, is a dual-polarized radar transmitting at 5.6 GHz with a 10 kHz PRF. Its range resolution is 0.60 m, and the acquisition duration is 1.6 s. The three systems were located at an altitude of about 50 m and were pointing toward the sea at different grazing and azimuth angles. Average sea states were approximately 3–4 on the Douglas scale. Environmental and oceanographic conditions were recorded by the WTD71 RV-PLANET ship during the experiment, providing in particular the surface height, the dominant wave time period, and the wind direction. For more details about MARLENE experiment the reader can refer to Fabbro et al. (2017).

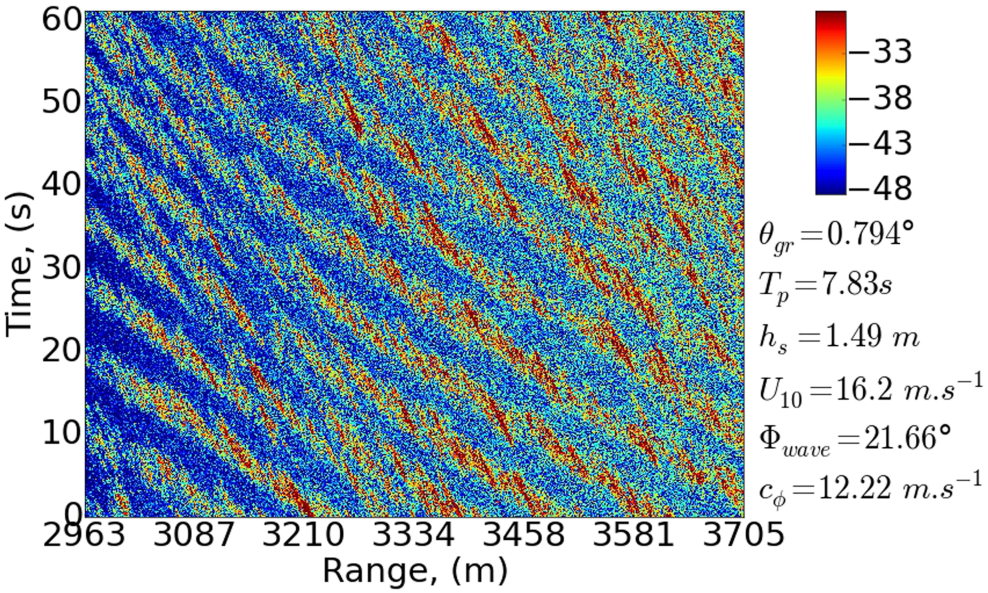

Figure 2. Space-time series of backscattered power (NRCS), in logarithmic scale, acquired by the MEMPHIS radar (35 GHz). The wind speed is U_{10} = 16.2 m/s, and sea wave conditions are similar to Figure 1.

Range-time series of the backscattered electric field were recorded with grazing angles below 2°. Two examples of range-time maps of backscattered power (NRCS) are presented in Figures 1 and 2 for the two radar systems MARSIG and MEMPHIS. The modulation by sea waves, as well as the almost periodic occurrence of high levels of NRCS, can be observed in these figures. The duration of the acquisition is approximately 60 s for both radars, while the illuminated areas are 338 and 742 m long in range for MARSIG and MEMPHIS, respectively. These characteristics are providing well-resolved dispersion diagrams, without aliasing. The two spectra obtained from Figures ?? and 2 are plotted in Figures 3 and 4. The dispersion relation of gravity waves is marked with a solid line, and the group line area is emphasized with the dotted line. A rough estimation of the slope of the group line, if considered as a straight piece of line, remains difficult. Therefore, a generic method allowing one to compute the slope of the group line has been proposed in Platzer

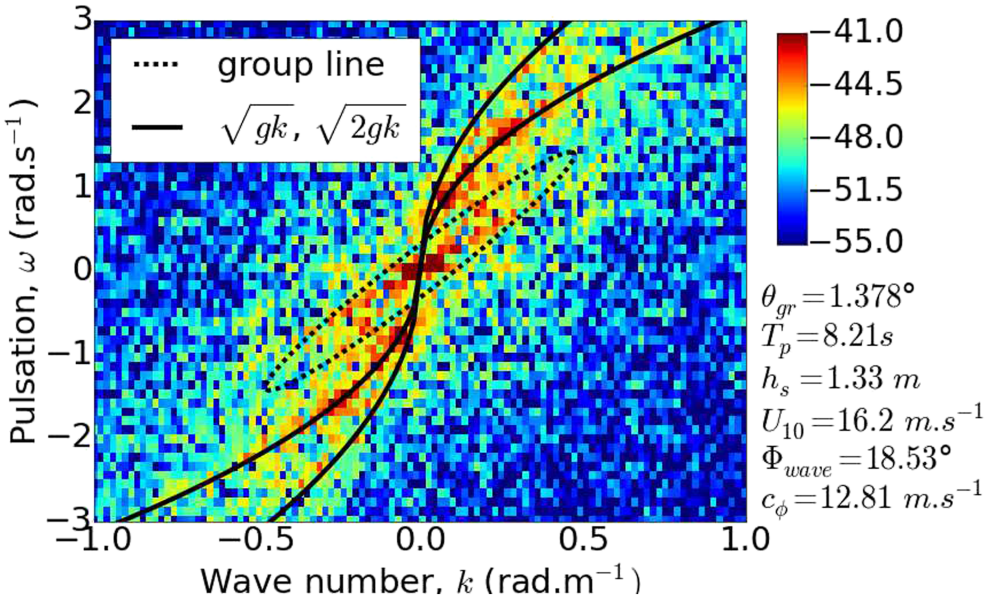

Figure 3. Dispersion diagram of the backscattered power (NRCS) plotted in Figure 1, in logarithmic scale, acquired by the MARSIG radar (14 GHz). The wind speed is U_{10} = 16.2 m/s.

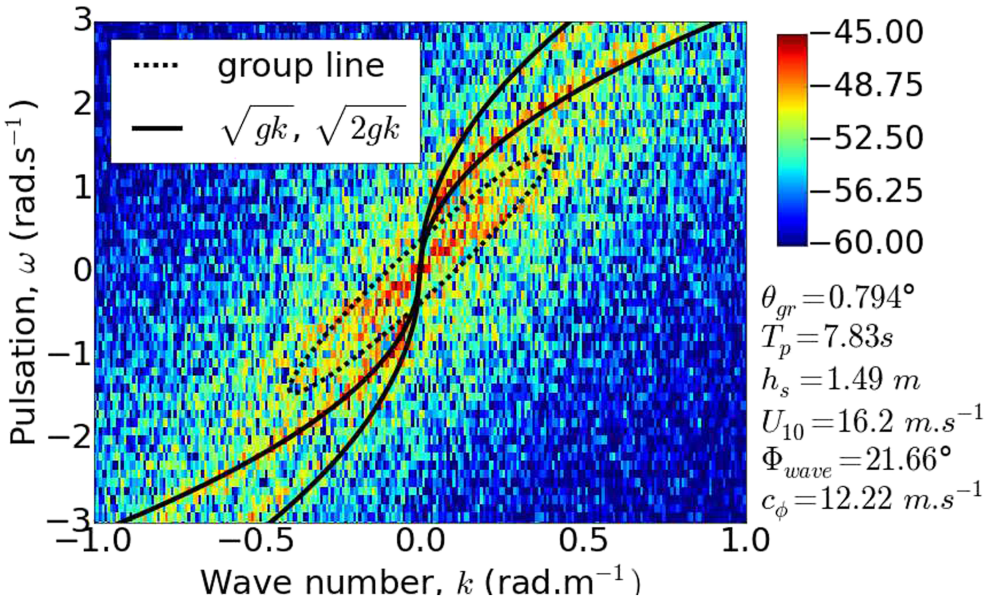

Figure 4. Dispersion diagram of the backscattered power (NRCS) plotted in Figure 2, in logarithmic scale, acquired by the MEMPHIS radar (35 GHz). The wind speed is $U_{10} = 16.2$ m/s, and sea wave conditions are similar to Figure 3.

et al. (2019). Section 3 introduces this method and applies it to experimental data. Other results of interest that stemmed from this method are presented in section 4.

3. Study of the Slope of the Group Line

In this section a focus on the modeling of the group line and on the estimation of its slope is proposed. Section 3.1 introduces briefly the theoretical model. The numerical simulations used for comparison with experimental data are presented in section 3.2.

3.1. Analytic Model and Numerical Simulations of the Group Line

In Platzer et al. (2019), it has been shown that any quadratic function of surface height generates a group line that covers a part of the space-time frequency plane (k, ω). In the case of a radar pointing in the main direction of propagation of long waves, it is mainly concentrated between the lines $\omega_u = \sqrt{gK_u} - \sqrt{g(K_u - k)}$ and $\omega_p = \sqrt{g(K_p + k)} - \sqrt{gK_p}$, where K_p denotes the wavenumber of the most energetic wave and K_u is associated to the resolution in range, acting as high-frequency cutoff.

For each k, a weighted average value of ω has been calculated, in the case of a K^{-3} power law gravity wave spectrum, for two types of nonlinearities, namely, the square of the surface height η^2 and the square of its slope along the range direction η_x^2. In the latter case, the average frequency $\langle \omega_{\eta_x^2} \rangle(k)$ is given by

$$\langle \omega_{\eta_x^2} \rangle(k) = \frac{\omega_p - \omega_u}{\ln\left(\frac{\omega_p}{\omega_u}\right)}. \quad (1)$$

It has also been pointed out in Platzer et al. (2019) that the duration of recorded time series, typically 1 min here, does not provide a high enough resolution in frequency to accurately describe the group line. Therefore,

Table 1
Availability of Data Processing From the MARLENE Campaign

Radar	Polarization	Frequency spectrum	Doppler spectrum
MEDYCIS	HH/VV	5.6 GHz	Yes
MARSIG	HH	8/11/14/17 GHz	No
MEMPHIS	HH	35 GHz	Yes

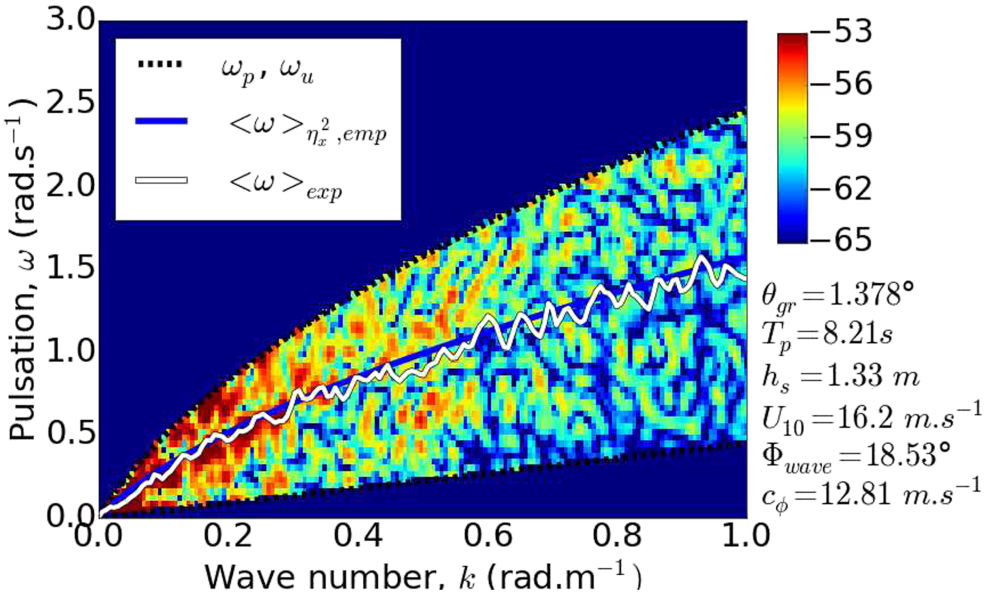

Figure 5. Group line, in logarithmic scale, of the dispersion diagrams plotted in Figure 3, from NRCS range-time maps acquired by the MARSIG radar (14 GHz). The blue line represents the average frequency predicted by equation (2), and the white line the one derived from the experimental group line.

an empirical formula has been established to take this inaccuracy into account, which predicts the average value that would be computed from a 2-D Fast Fourier Transform (FFT), namely,

$$\langle\omega_{\eta_x^2}\rangle_{emp}(k)=\frac{3}{5}\frac{\omega_p^{5/2}-\omega_u^{5/2}}{\omega_p^{3/2}-\omega_u^{3/2}}. \tag{2}$$

Similar results have been also derived for nonlinearities behaving as η^2. Once an average frequency has been derived, one can define an average slope of the group line as $<\omega>/k$, the slope of the line joining the origin to $(k,<\omega>)$. Such a slope, which depends on k, can be compared to velocities of waves.

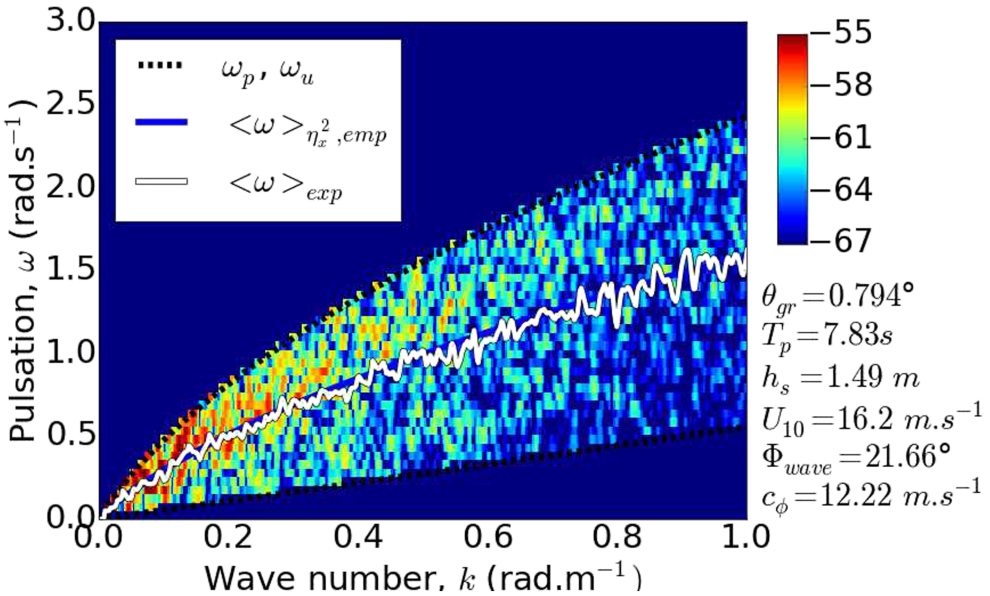

Figure 6. Group line, in logarithmic scale, of the dispersion diagrams plotted in Figure 4, from NRCS range-time maps acquired by the MEMPHIS radar (35 GHz). The blue line represents the average frequency predicted by equation (2), and the white line the one derived from the experimental group line.

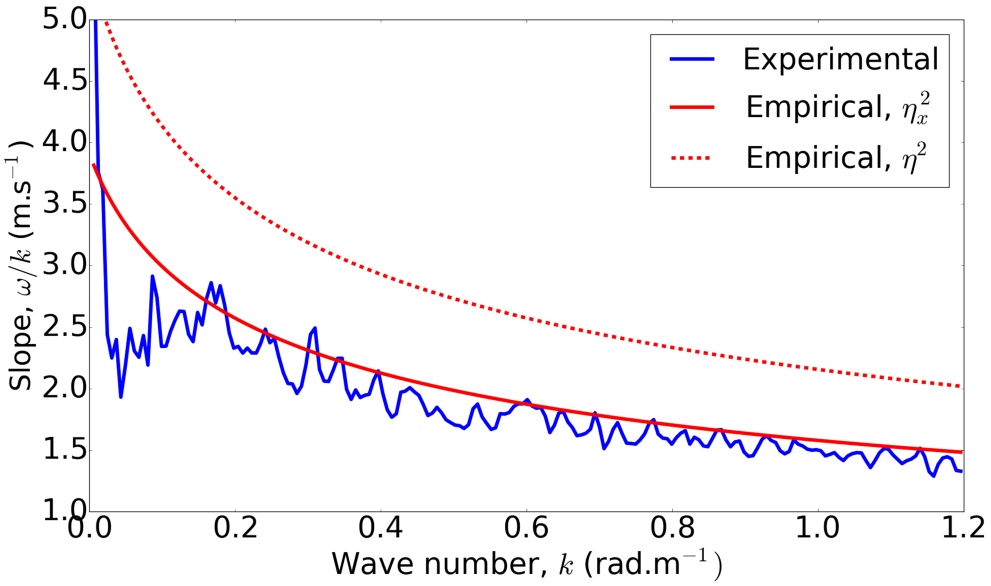

Figure 7. Comparison of the slopes of the group lines associated with η^2 and η_x^2, as predicted by the empirical formula, with the one derived from experimental data for the MARSIG NRCS data (14 GHz).

3.2. Behavior of Experimental Data

Let us now process the NRCS data in order to compare the group lines of the dispersion diagrams with theoretical results. A preliminary data processing is necessary to perform this comparison with good accuracy. Since the backscattered field is recorded at less than 1,000 radar cells in range, a zero-padding method is used to improve the wavenumber resolution of the 2-D FFT. In accordance with the theoretical results presented in Platzer et al. (2019), a mask is applied to filter out values of ω outside the interval $[\omega_u, \omega_p]$. The weighted average frequency of the group line is then derived from

$$\langle\omega\rangle(k) = \frac{\sum_{\omega} \omega\varphi(\omega, k)}{\sum_{\omega} \varphi(\omega, k)} \tag{3}$$

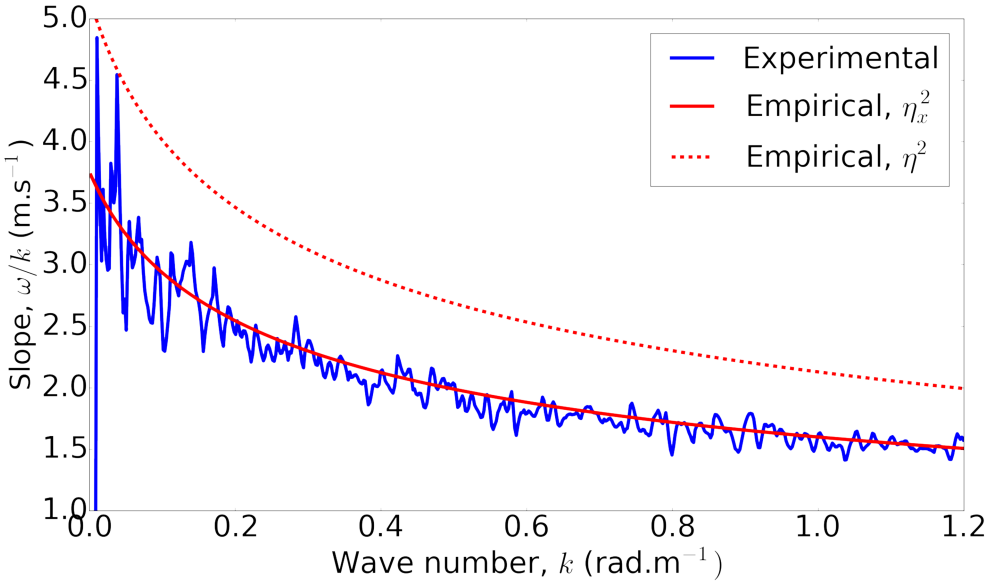

Figure 8. Comparison of the slopes of the group lines associated with η^2 and η_x^2, as predicted by the empirical formula, with the one derived from experimental data for the MEMPHIS NRCS data (35 GHz).

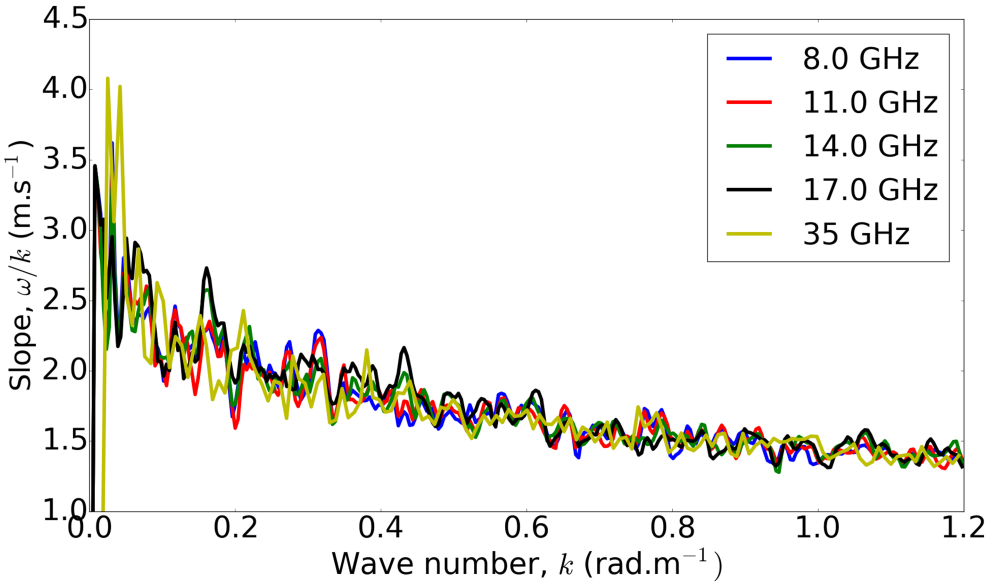

Figure 9. Comparison of the experimental slopes of the group lines for various frequencies acquired by the MARSIG and MEMPHIS radars at the same time with grazing angle of $\theta_{gr} = 0.91°$ and azimuth angles of 53°.

where $\varphi(k, \omega)$ is the cut of the dispersion diagram along the ω axis for a given wavenumber k. The results of the data processing of the two images presented in Figures 3 and 4 are exhibited in Figures 5 and 6.

The range resolutions are respectively 0.60 m for MARSIG and 0.75 m for MEMPHIS, leading to cutoff frequencies of approximately $K_u \simeq 10.5$ rad/m and $K_u \simeq 8.4$ rad/m. The wavenumber of the dominant wave, K_p, is estimated from the wave time period T_p recorded during the experiment. After dividing by k, the mean frequencies plotted in Figures 5 and 6 are transformed into slopes in Figures 7 and 8, where experimental results are compared to the slopes derived from the empirical formula (2) with the same parameters K_p and K_u. Except at low wavenumbers ($k < 0.1$ rad/m), where small fluctuations of $< \omega >$ generate strong fluctuations of the slope, experimental curves and equation (2) almost coincide and have the same decreasing behavior. The slight difference could result from the azimuth angle between the radar and the sea waves direction that is close to 20° in these cases, while the empirical formulas assume a one-dimensional configuration. The figures also show that the experimental slopes are significantly lower than the slope associated with η^2.

These results suggest that the group line is shaped by the universal behavior of the backscattering amplitude from a rough surface at low grazing angle Tatarskii and Charnotskii (1998), which predicts it is proportional to the square of the vertical component of the incident wavevector, q_0. If applied to each radar cell, the local grazing incidence can be approximated by a linear function of the slope of the long gravity waves η_x, and the nonlinear term of lowest order of q_0^2 (or q_0^4 for NRCS) is thus proportional to η_x^2.

The method presented in this section can be applied in a more exhaustive way to the data of the MARLENE campaign. In particular, it allows one to study frequency and azimuth dependence, as presented below in sections 3.3 and 3.4.

3.3. Frequency Invariance

The MARSIG radar, as described in section 2, is operating simultaneously at four frequencies (8, 11, 14, and 17 GHz). In addition, the acquisitions of the MEMPHIS radar (35 GHz) were almost simultaneous with those of the MARSIG radar (less than 1 min gap). It slightly differs in the range excursion, but the sea states are the same. This allows us to compare the experimental results obtained from MARSIG and MEMPHIS radars for the same grazing and azimuth angles, the latter being a measurement of the angle between the radar pointing direction and the dominant sea waves direction of propagation.

Figures 9 and 10 present the results of the comparison of simultaneous acquisitions by the radar systems for two different azimuth angles. In both figures, the slopes of the group lines at all frequencies coincide, up to

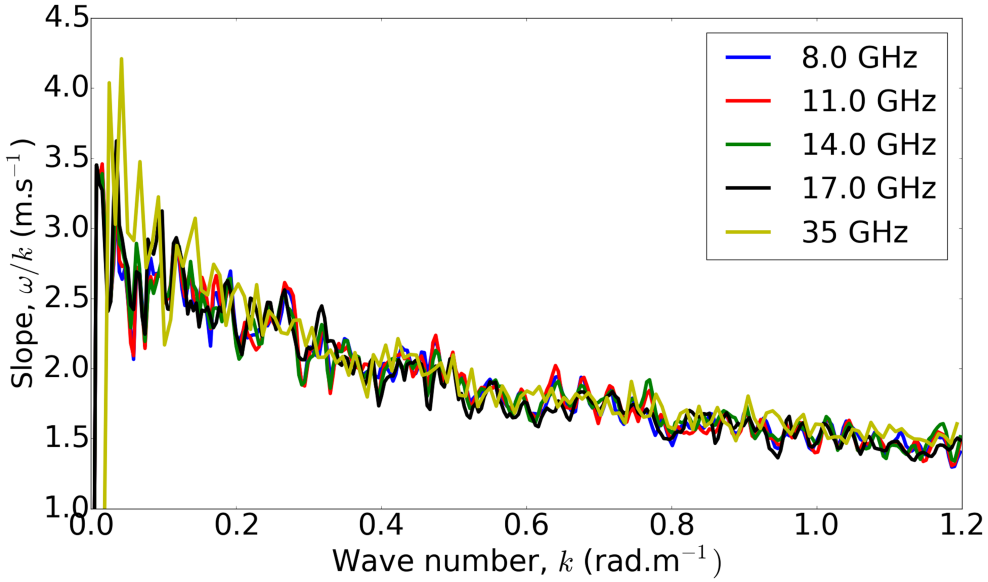

Figure 10. Comparison of the experimental slopes of the group lines for various frequencies acquired by the MARSIG and MEMPHIS radars at the same time with grazing angle of $\theta_{gr} = 0.91°$ and azimuth angles of 21°.

fluctuations of small amplitude (less than 0.1 m/s. This shows that the slope of the group line is independent of the radar frequency, in accordance with the proposed models, which only refer to the spectrum of gravity waves and to the radar resolution in range.

3.4. Azimuth Angle Dependence

Let us recall that here the azimuth angle denotes the angle between the backscattered electromagnetic wavevector and the wavevector of the most energetic gravity waves. Indeed, in the coastal conditions encountered here, the wind direction differs significantly from the main direction of propagation of long waves. Therefore, up-wave conditions correspond to azimuth angle equal to 0. A careful analysis of Figures 9 and 10, corresponding to different azimuth angles, shows that the slopes of the group lines for 21° are higher

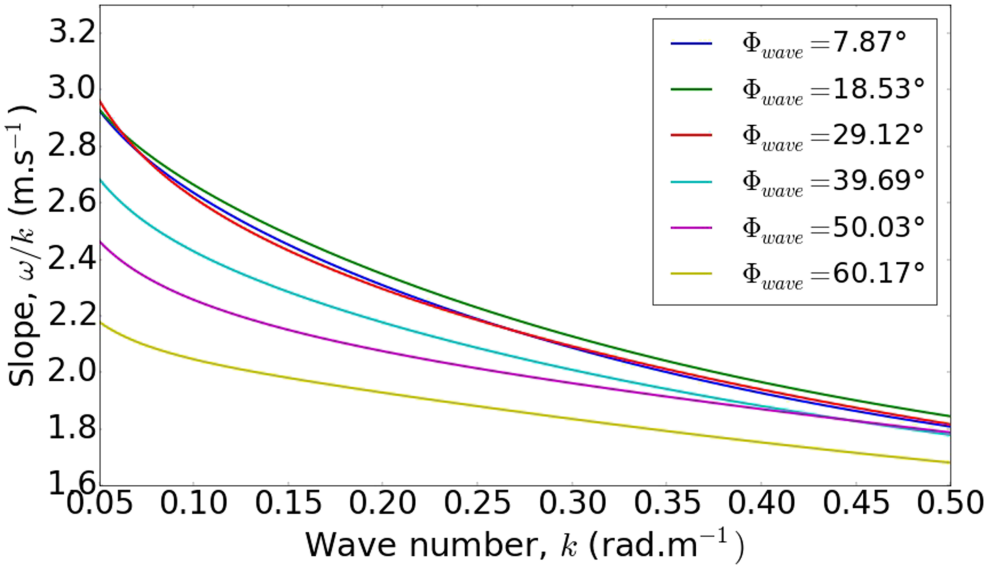

Figure 11. Comparison of the slopes of group lines for the same grazing incidence but different azimuth angles for the MARSIG radar (14 GHz).

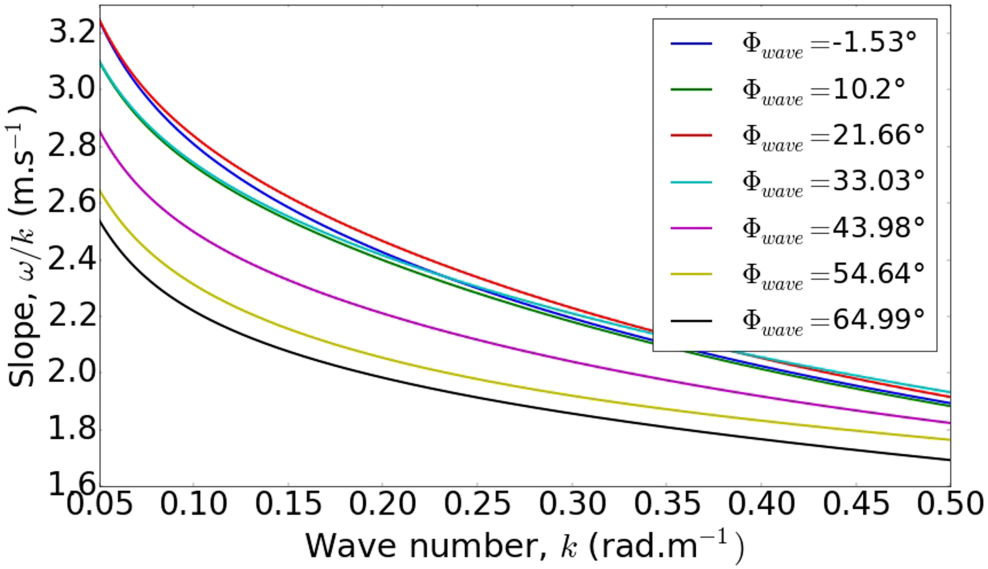

Figure 12. Comparison of the slopes of group lines for the same grazing incidence but different azimuth angles for the MEMPHIS radar (35 GHz).

than for 53°. Contrary to radar frequency, the direction of propagation of long waves has an impact on the group line.

During the MARLENE campaign, the acquisitions were performed following a predefined pattern of radar pointing directions (see Figure 1 in Fabbro et al. (2017)). For each grazing angle, six or seven measurements of sea clutter have been performed for various azimuth angles. The corresponding NRCS maps acquired have been processed. The slopes of the group lines are reported in Figures 11 and 12. For a better visualization, the curves in the figures are polynomial fits of the estimated slopes. These two figures show that the larger the azimuth angle, the lower the slope of the group line. For azimuth angles below 30°, the slope remains almost unchanged. This completes the justification of the use of a one-dimensional model in Platzer et al. (2019) to predict the characteristics of the group lines in up-wave conditions.

For large azimuth angles, the group line is still observable, even though the energy in first-order dispersion relation is drastically reduced, as already pointed out in Figure 4 of Plant and Farquharson (2012). Though we have no model at hand to explain the decaying behavior of the slope with azimuth angle, it has to be noticed that for large azimuth angles the combination of two gravity waves with wavevectors of same magnitude, thus with same frequency but different directions of propagation, may contribute to the group line at $(k, 0)$. This emphasizes that the area of the (k, ω) plane located below $\omega = \omega_u$, which represents the lower boundary of the group line in a one-dimensional configuration, is filled up when the azimuth angle increases. Though not quantified here, this can explain the decreasing behavior of the slope of the group line.

Thereafter, the calculation of the slope of the group line has been performed for each NRCS range-time map of the database. For a clear representation, the value of each slope is given for a single value of k, $k = 0.2$ rad/m being chosen as a compromise between avoiding the impact of the fluctuations at very low values of k and ensuring a high signal-to-noise ratio. Results are presented in Figure 13. The horizontal axis refers to the phase velocity of the dominant wave, $c_p = \sqrt{g/K_p}$. K_u is determined by the size of the radar cells. The slopes reported in the figure are obtained for azimuth angles varying from 0° up to almost 90°. This figure exhibits the variation of the slope of the group line with respect to both the azimuth angle and the weather conditions. It emphasizes that the empirical model assuming a nonlinear dependence as η_x^2, represented by the blue curve, matches well with measurements at low azimuth angles. It must also be noticed that the results remain very similar if the slopes are estimated at $k = 0.1$ rad/m or $k = 0.3$ rad/m. Some points of Figure 13 with low azimuth angles, represented in blue color, are lower than expected. This is due to a change in the environmental condition during the measurement campaign. Hence, the decrease of the significant wave height on the second day has a light impact on the slope of the group line, lowering it.

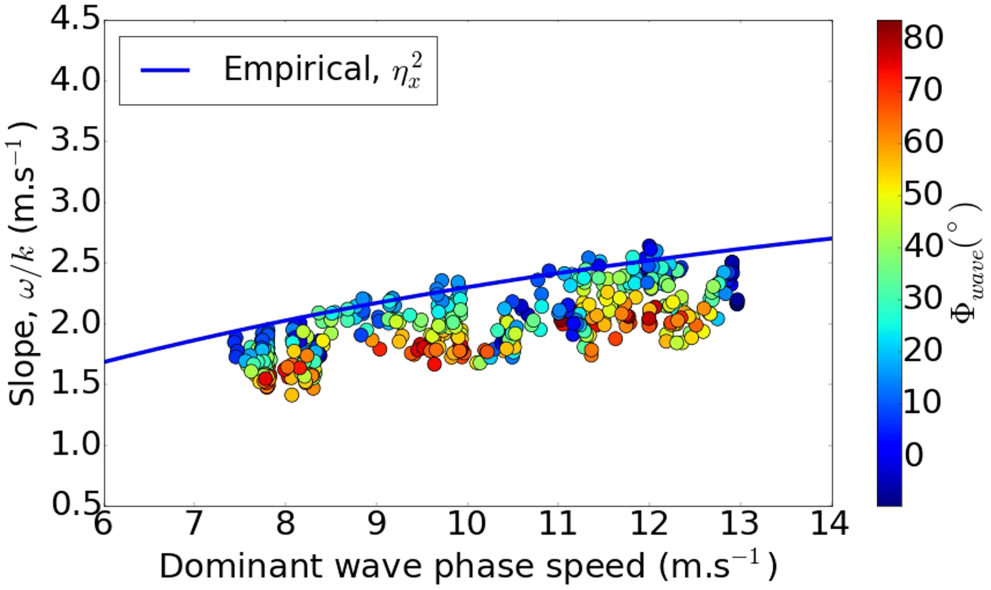

Figure 13. Scatterplot of the slopes of group lines from the data acquired by the MARSIG radar (14 GHz) and the MEMPHIS radar (35 GHz). The slopes are estimated at the value of $k = 0.2$ rad/m.

4. Analysis of Experimental Results

The slope of the group line, $\langle\omega\rangle/k$, can be interpreted as a velocity. This section focuses on the comparison with other velocities, such as the ones derived from Doppler shifts. With this aim, section 4.1 is dealing with the dispersion diagram of the Doppler velocity field. Since sea spikes are generally related to large Doppler velocities and to breaking waves, a comparison between the slopes of the group line with an empirical law for the velocity of breakers is achieved in section 4.3.

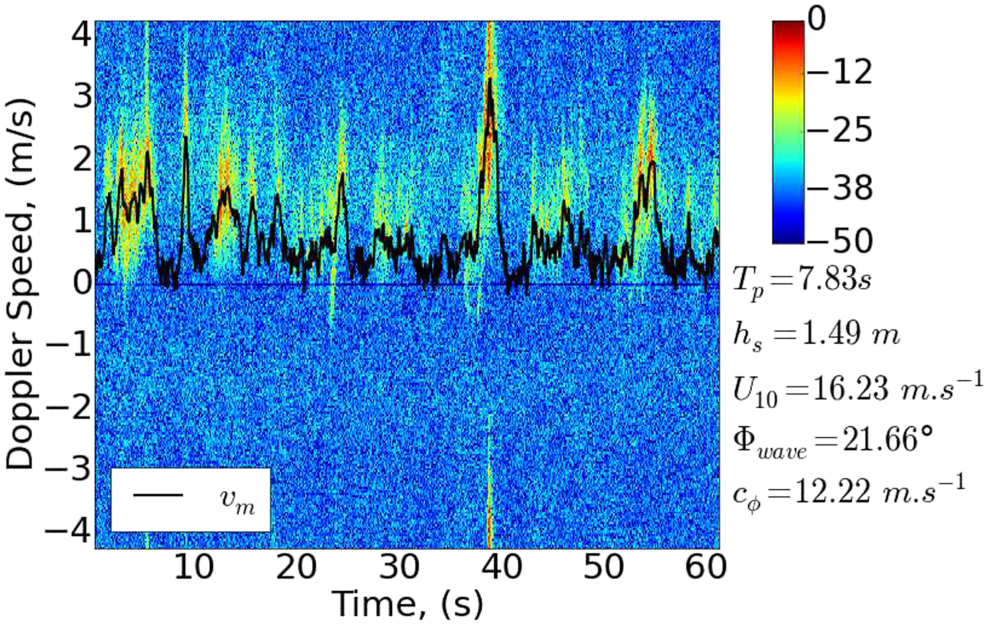

Figure 14. Example of a temporal spectrogram, normalized by its maximum, of the time series of the backscattered field from a single radar cell acquired by the MEMPHIS radar (35 GHz). The black line represents the mean Doppler velocity.

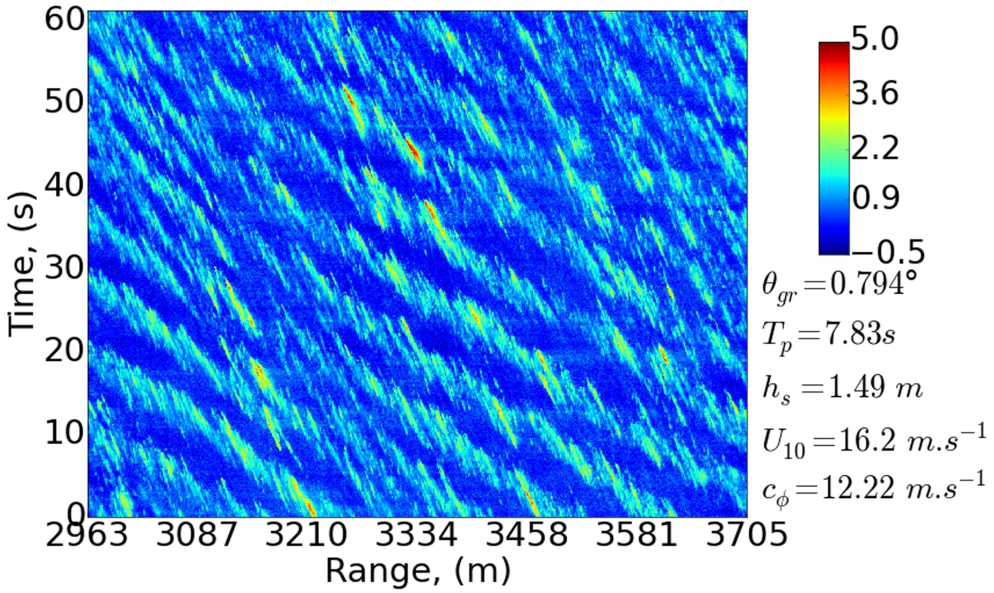

Figure 15. Range-time map of Doppler velocity field represented in color scale (in m/s) associated to the NRCS range-time map in Figure 2 acquired by the MEMPHIS radar (35 GHz).

4.1. Dispersion Diagram of Doppler Velocities Field

In Smith et al. (1996) and Plant and Farquharson (2012), dispersion diagrams are computed from the range-time series of the local Doppler velocity field, instead of NRCS. The use of Doppler velocity, when available, is more popular since, in the frame of linear theory, its spectrum is linked to that of surface height in a simple way. Below, the dispersion diagrams associated with Doppler velocity and NRCS are compared, since MEMPHIS data acquired during MARLENE experiment enable the study of both Doppler spectra and dispersion diagrams. The computation of the velocity is realized using a spectrogram approach by Fourier transform. The spectrogram is computed from the complex backscattered field of each radar range cell, integrating over a window of 128 s sliding with a time shift of $\delta t = 0.05$ s. An example of spectrogram is reported in Figure 14. This representation shows the temporal variation of the Doppler velocity. The mean Doppler frequency, f_c, defined as the first normalized momentum of each Doppler spectrum, $\Psi(f)$, is derived as a

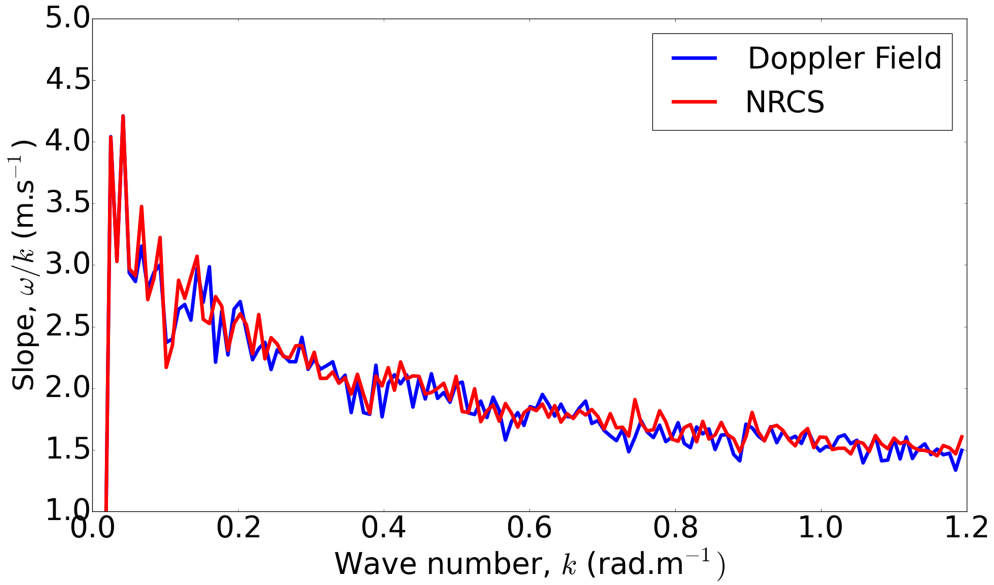

Figure 16. Comparison of the slopes of the group lines from the range-time map of NRCS (Figure 2) and Doppler velocity field (Figure 15) issued from the same backscattered field acquired by the MEMPHIS radar (35 GHz).

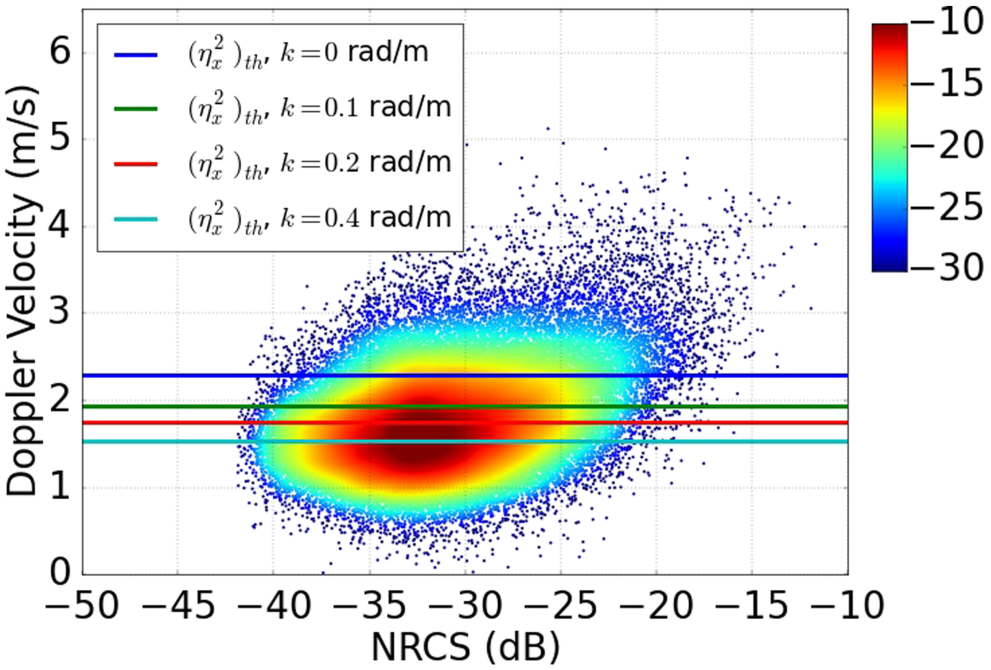

Figure 17. Relation between the level of NRCS from Figure 2, in logarithmic scale, and Doppler velocities from Figure 15. The normalized cross distribution between NRCS and Doppler velocities is represented by the color map in logarithmic scale. The analytic formula of the η_x^2 dispersion diagram group line slope is drawn for various values of k (blue line: $k = 0$ rad/m, green line: $k = 0.1$ rad/m, red line: $k = 0.2$ rad/m, cyan line: $k = 0.4$ rad/m).

function of time,

$$f_c = \frac{\int f\Psi(f)df}{\int \Psi(f)df} \tag{4}$$

and is transformed into mean velocity. Figure 15 shows the Doppler velocity field associated to the same MEMPHIS radar acquisition as the NRCS map presented in Figure 2 and with the same dimensions. Both maps enable the computation of a dispersion diagram.

The comparison of the slopes of the group lines obtained from the NRCS map and from the Doppler velocity map is shown in Figure 16. The slopes are similar over the whole range of wavenumbers, even when the group line becomes undetectable. This result has already been exhibited by Frasier and McIntosh in X band Frasier and McIntosh (1996). These observations are suggesting that the local Doppler velocity and the local NRCS are providing the same group lines. This is not expected if the Doppler velocity is considered as a measurement of the orbital velocity and if one refers to the linear theory of gravity waves. In this frame, the spectrum of the orbital velocity decays faster than that of surface slope but slower than that of surface height. Consequently, the slope of the group line associated to Doppler velocity should behave in between the two Platzer et al. (2019). This is clearly not the case, and it is concluded that the Doppler velocity cannot be simply related to surface parameters, even though its group line coincides with that associated to η_x^2. Some studies have related steepening waves with strong Doppler velocities Jessup et al. (1991), Holliday et al. (1998), but no analytical model can currently explain this behavior.

4.2. Slope of the Group Line Versus Doppler Velocity

The computation of the Doppler velocity allows one to study the relationship between the level of NRCS of each pixel (represented in Figure 2) with the associated Doppler velocity (represented in Figure 15). The normalized cross distribution between NRCS and Doppler velocities is represented by the color map in Figure 17. Doppler velocities for very low NRCS levels are discarded for the cross distribution because of the low signal-to-noise ratio in those areas. The cross distribution is then representative of the crest behavior, and the NRCS dynamic range is around 30 dB. Fast scatterers are observable in the high-velocity range, up to 5 m/s, associated to high NRCS levels. But the fastest components do not exactly coincide with the brightest. This representation could question the sea spikes behavior since high velocities can be found for

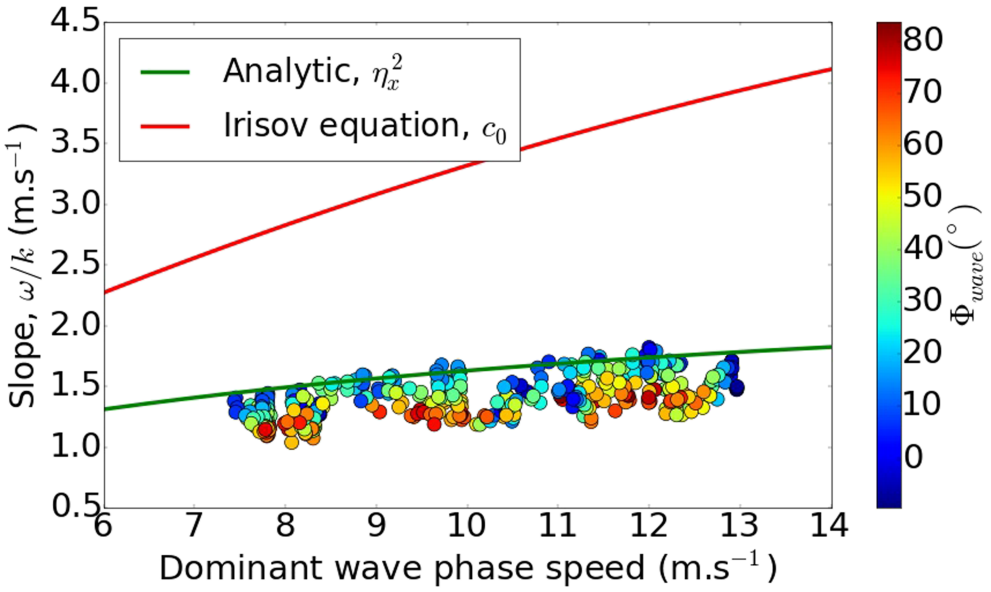

Figure 18. Slopes of the group lines (wave-radar relative azimuth direction in color scale) for the data acquired by the MARSIG radar (14 GHz) and the MEMPHIS radar (35 GHz), corrected of the FFT impact and compared to the equations (5) and (1) in red and green line respectively. The slopes are estimated at the value of $k = 0.2$ rad/m.

moderate level of NRCS. The analysis proposed here is limited to HH polarization, but similar representations and remarks are given in Yurovsky et al. (2018) for high grazing angles, considering both HH and VV polarization.

To compare the Doppler velocities with the theoretical estimation of the slope of the group line associated to η_x^2 equation(1), the latter has also been plotted in Figure 17 for various values of k, from 0 up to 0.4 rad/m, 0.4 rad/m corresponding to the typical limit of detectability of the group line. It shows that the analytical group line associated to η_x^2 does not match the fastest Doppler velocities. The slope of the group line of the Doppler field dispersion diagram is greater than the average velocity of the cross distribution (1.72 m/s here) but is of same order of magnitude as the NRCS-weighted average velocity (2.06 m/s). However, the average Doppler velocity of sea spikes is strongly fluctuating from one sample to another, between 1.71 and 2.66 m/s for the 57 maps recorded in similar sea conditions, while the slope of the group line remains very stable. In addition, their behavior with respect to azimuth angle strongly differ. The average Doppler velocity roughly behaves as a cosine function when the slope of the group line is only slightly reduced at large angles (Figure 18). Therefore, we have not been able to establish a clear quantitative relationship between the statistical characteristics of the Doppler velocity field and the slope of the group line.

4.3. Slope of the Group Line Versus Velocity of Breakers

In the literature, the large Doppler velocities are related to sea spikes and are often linked to steepening and breaking waves Hwang et al. (2008), Frasier et al. (1998), Holliday et al. (1998). Irisov, in Irisov and Plant (2016), has proposed an empirical formula to estimate the mean velocity of breakers:

$$c_0 = 0.22 + 0.39c_d - 0.008c_d^2, \tag{5}$$

where c_d is the phase velocity of the most energetic wave. This formula is based on data gathered in Plant (2012). For a phase velocity of about 12 m/s, the mean breaker velocity is 3.75 m/s which corresponds to the Doppler velocities of the few fastest scatterers observable in the MARLENE database (see Figure 17).

Irisov's formula can be compared to the analytic formulation of the slope of the group line as well. For that purpose, the values of experimental slopes of the group lines reported in Figure 13 are corrected with a factor calculated from the ratio of the equations (1) and (2). This correction is necessary to remove the bias induced by the 2-D FFT when computing the group line. The result is presented in Figure 18. The measurements considered to establish this graph are corresponding to several frequencies in X band to Ka band and a large range of azimuth angles and dominant sea wave velocities. This figure shows that the slopes of the group

lines are much lower than the mean velocity of breakers. Hence, this observation suggests that the group lines generated by the data from MARLENE campaign are not the signature of breaking events.

5. Discussion and Conclusion

Some results about dispersion diagrams obtained by applying a two-dimensional Fourier transform to radar returns acquired by high-resolution radar systems have been presented in this paper and in the companion paper Platzer et al. (2019). In the latter, a way to estimate the slope of the group line has been proposed and applied here to the experimental data acquired during the MARLENE campaign Fabbro et al. (2017). It appears that the group line of the dispersion diagram obtained from the backscattered amplitude behaves as the one obtained from the dispersion diagram of the square of the slope of the sea surface η_x^2. Moreover, it has been shown that the group line is invariant with respect to the radar frequency but depends on the azimuth angle between the radar pointing direction and the sea waves direction. These results suggest that the impact on the group line of electromagnetic scattering under grazing incidence is described by the local grazing angle, as suggest by Frasier and McIntosch Frazier and McIntosh (1996). Small height perturbation theory, though not applicable here, leads to the same behavior but underestimates the associated energy Plant and Farquharson (2012). Shadowing functions also ensure a nonlinear behavior of the scattering amplitude with respect to surface height, but, to our knowledge, none of them is consistent with the asymptotic behavior at grazing predicted by Maxwell equations, which is a major drawback in the present experimental conditions.

Then, an analysis of local Doppler velocities has been carried out. It has been observed that the associated slope of the group line is the same as the one derived from the NRCS and that it does not fit the large Doppler velocities related to sea spikes. The empirical law of equation (5), proposed to predict the most probable velocity of breakers, does not match either. Its predictions by far exceed the experimental values of the slope of the group line. The latter is thus not a good estimation of the velocity of breaking waves. If sea spikes are local events with short space and time coherence lengths, it can be expected that a two-dimensional Fourier transform with large time and range acquisition spreads out the associated energy, and thus sea spikes do not significantly impact the characteristics of the group line. No focus on the group line from optical measurements has been made in the literature. Thus, it could be interesting now to compare the results obtained on the present paper on the group line with data from optical or video systems which are widely used henceforth by the community.

Acknowledgments
The authors acknowledge the Délégation Générale de l'Armement (DGA) for financial support and Gabriel Soriano, at Institut Fresnel, for valuable discussions and for providing the computer code devoted to solving the scattering problem. The data used in the paper are not available publicly. These are the property of Fraunhofer FHR, WTD71, and ONERA. Please contact the authors at vincent.fabbro@onera.fr for more information.

References

Borge, J. N., Reichert, K., & Hessner, K. (2013). Detection of spatio-temporal wave grouping properties by using temporal sequences of X-band radar images of the sea surface. *Ocean Modelling*, *61*, 21–37. https://doi.org/10.1016/j.ocemod.2012.10.004

Creamer, D. B., Henyey, F., Schult, R., & Wright, J. (1989). Improved linear representation of ocean surface waves. *Journal of Fluid Mechanics*, *205*, 135–161. https://doi.org/10.1017/S0022112089001977

Dankert, H., Horstmann, J., & Rosenthal, W. (2005). Wind- and wave-field measurements using marine X-band radar-image sequences. *IEEE Journal of Oceanic Engineering*, *30*(3), 534–542. https://doi.org/10.1109/JOE.2005.857524

Donelan, M. A., Hamilton, J., Hui, W. H., & Stewart, R. W. (1985). Directional spectra of wind-generated ocean waves. *Philosophical Transactions of the Royal Society of London Series A, Mathematical and Physical Sciences*, *315*(1534), 509–562. https://doi.org/10.1098/rsta.1985.0054

Fabbro, V., Biegel, G., Förster, J., Poisson, J. B., Danklmayer, A., Böhler, C., et al. (2017). Measurements of sea clutter at low grazing angle in Mediterranean coastal environment. *IEEE Transactions on Geoscience and Remote Sensing*, *55*(11), 6379–6389. https://doi.org/10.1109/TGRS.2017.2727057

Frasier, S., & McIntosh, R. (1996). Observed wavenumber-frequency properties of microwave backscatter from the ocean surface at near-grazing angles. *Journal of Geophysical Research*, *101*(C8), 18,391–18,407. https://doi.org/10.1029/96JC01685

Frasier, S. J., Liu, Y., & McIntosh, R. E. (1998). Space-time properties of radar sea spikes and their relation to wind and wave conditions. *Journal of Geophysical Research*, *103*(C9), 18,745–18,757. https://doi.org/10.1029/98JC01456

Frazier, S. J., & McIntosh, R. E. (1996). Observed wavenumber-frequency properties of microwave backscatter from the ocean surface at near-grazing angles. *Journal of Geophysical Research*, *101*(C8), 18,391–18,407.

Holliday, D., DeRaad, L. L., & St-Cyr, G. J. (1998). Sea-spike backscatter from a steepening wave. *IEEE Transactions on Antennas and Propagation*, *46*(1), 108–113. https://doi.org/10.1109/8.655457

Hwang, P. A., Sletten, M. A., & Toporkov, J. V. (2008). Analysis of radar sea return for breaking wave investigation. *Journal of Geophysical Research*, *113*, C02003. https://doi.org/10.1029/2007JC004319

Irisov, V., & Plant, W. (2016). Phillips' lambda function: Data summary and physical model. *Geophysical Research Letters*, *43*(5), 2053–2058. https://doi.org/10.1002/2015GL067352

Jessup, A. T., Melville, W. K., & Keller, W. C. (1991). Breaking waves affecting microwave backscatter: 1. Detection and verification. *Journal of Geophysical Research*, *96*(C11), 20,547–20,559. https://doi.org/10.1029/91JC01993

Krogstad, H. E., & Trulsen, K. (2010). Interpretations and observations of ocean wave spectra. *Ocean Dynamics*, *60*(4), 973–991. https://doi.org/10.1007/s10236-010-0293-3

Miret, D., Soriano, G., Nouguier, F., Forget, P., Saillard, M., & Guérin, C. A. (2014). Sea surface microwave scattering at extreme grazing angle: Numerical investigation of the doppler shift. *IEEE Transactions on Geoscience and Remote Sensing*, *52*(11), 7120–7129. https://doi.org/10.1109/TGRS.2014.2307893

Miret, D., Soriano, G., & Saillard, M. (2014). Rigorous simulations of microwave scattering from finite conductivity two-dimensional sea surfaces at low grazing angles. *IEEE Transactions on Geoscience and Remote Sensing*, *52*(6), 3150–3158. https://doi.org/10.1109/TGRS.2013.2271384

Phillips, O. M. (1985). Spectral and statistical properties of the equilibrium range in wind-generated gravity waves. *Journal of Fluid Mechanics*, *156*, 505–531. https://doi.org/10.1017/S0022112085002221

Plant, W. J. (2012). Whitecaps in deep water. *Geophysical Research Letters*, *39*(16). https://doi.org/10.1029/2012GL052732, l16601

Plant, W. J., & Farquharson, G. (2012). Origins of features in wave number-frequency spectra of space-time images of the ocean. *Journal of Geophysical Research*, *117*, C06015. https://doi.org/10.1029/2012JC007986

Platzer, F., Saillard, M., & Fabbro, V. (2019). Two-dimensional spectra of radar returns from sea: 1. Theoretical and numerical study of the group line. *Journal of Geophysical Research: Oceans*, *124*. https://doi.org/10.1029/2019JC015121

Rino, C., Eckert, E., Siegel, A., Webster, T., Ochadlick, A., Rankin, M., & Davis, J. (1997). X-band low-grazing-angle ocean backscatter obtained during logan 1993. *IEEE Journal of Oceanic Engineering*, *22*(1), 18–26. https://doi.org/10.1109/48.557536

Smith, M., Poulter, E., & McGregor, J. (1996). Doppler radar measurements of wave groups and breaking waves. *Journal of Geophysical Research*, *101*(C6), 14,269–14,282. https://doi.org/10.1029/96JC00766

Stevens, C. L., Poulter, E. M., Smith, M. J., & McGregor, J. A. (1999). Nonlinear features in wave-resolving microwave radar observations of ocean waves. *IEEE Journal of Oceanic Engineering*, *24*(4), 470–480. https://doi.org/10.1109/48.809268

Tatarskii, V. I., & Charnotskii, M. I. (1998). On the universal behavior of scattering from a rough surface for small grazing angles. *IEEE Transactions on Antennas and Propagation*, *46*(1), 67–72. https://doi.org/10.1109/8.655452

Young, I. R., Rosenthal, W., & Ziemer, F. (1985). A three-dimensional analysis of marine radar images for the determination of ocean wave directionality and surface currents. *Journal of Geophysical Research*, *90*(C1), 1049–1059. https://doi.org/10.1029/JC090iC01p01049

Yurovsky, Y. Y., Kudryavtsev, V. N., Chapron, B., & Grodsky, S. A. (2018). Modulation of ka-band doppler radar signals backscattered from the sea surface. *IEEE Transactions on Geoscience and Remote Sensing*, *56*(5), 2931–2948. https://doi.org/10.1109/TGRS.2017.2787459